Multi-scale and multi-physics simulation of central segregation in an equiaxed dendritic mushy zone during continuous casting of steel

Y. Feng, B.G. Thomas, J. Sengupta, Miha Založnik, A.B. Phillion

Multi-scale and multi-physics simulation of central segregation in an equiaxed dendritic mushy zone during continuous casting of steel

Y. Feng[1,3], B.G. Thomas[2], J. Sengupta[3], M. Založnik[4], A.B. Phillion[1*]

[1] *Department of Materials Science and Engineering, McMaster University, Hamilton, Canada*

[2] *Department of Mechanical Engineering, Colorado School of Mines, Golden, USA*

[3] *Global R&D Hamilton ArcelorMittal Dofasco, Hamilton, Canada*

[4] *Université de Lorraine, CNRS, IJL, F-54000 Nancy, France*

Abstract

Centreline segregation during continuous casting of steel is highly detrimental to the end-product mechanical properties. In this study, a 3D multi-scale and multi-physics model is developed and validated that directly predicts alloy segregation occurring in peritectic steel grades having centreline equiaxed grain morphology. The model consists of four models: (1) a 1D macroscale heat transfer and solidification model, (2) a 3D mesoscale dendritic solidification model, (3) a 3D mesoscale dendritic fluid flow model, and (4) a 3D mesoscale solute transport and redistribution model. The use of a mesoscale domain where the solid and liquid phases are separately discretized allows for consideration of physical phenomena affecting segregation that are classically hidden by the averaging procedures of fully continuum approaches. Thus the new model is able to account for the multiple phenomena occurring during continuous casting while also directly considering the stochastic effects resulting from grains having randomly-placed nuclei as well as interactions between the liquid and solid phases. The results demonstrate that solute partitioning combined with intra-dendritic fluid flow leads eventually to liquid channels enriched with solute that result in centreline segregation. The predicted composition in these discrete liquid channels shows excellent agreement with a Mn centreline segregation profile experimentally-measured via microscopic X-Ray fluorescence of a commercially-cast steel slab. Finally, the effects of alloy composition, and soft reduction on the degree of centreline segregation are examined.

Keywords: centreline segregation, solidification, intra-dendritic flow model, equiaxed microstructure.

1. Introduction

Inhomogeneity in the distribution of solute within a metallic alloy during casting results in a severe defect known as macrosegregation. This defect is a result of three fundamental mechanisms: (1) Solute enrichment of the liquid as a result of solute partitioning during solidification; (2) Flow of solute-enriched liquid through the mushy zone containing solidifying dendrites and (3) Transport of solid grains or grain fragments throughout the liquid pool [1]. Other relevant phenomena include interdendritic fluid flow caused by solidification shrinkage [2], temperature changes in liquid density [3], mechanical deformation [4] and electromagnetic forces [5].

Macrosegregation along the centreline of a cast product, known as centreline segregation, is one of the most detrimental defects in steelmaking because it cannot be removed. Due to the large length scales involved, it is simply not possible to achieve chemical homogeneity through downstream processing. Macrosegregation acts as initiation sites for cracking and porosity [6], as well as also leading to stray grain formation that results in reduced mechanical properties. Although strategies such as electromagnetic stirring, soft reduction and intense cooling have been used to lessen macroseg-

Preprint version of published article.
Cite as: Y. Feng et al., *Materialia* **33** (2024), 102003.
DOI: 10.1016/j.mtla.2023.102003

regation [7], great interest remains in better understanding and minimizing this defect [8].

Experimental investigation [9, 10, 11, 12, 13, 14, 15, 16] has provided much quantitative characterization of macrosegregation. X-ray fluorescence (XRF) spectroscopy analysis is a well-established method for elemental analysis of a great variety of specimens. The advantages of the non-destructive or poorly destructive character and the ability to conduct simultaneous multi-element determinations with high sensitivity have made it applicable for the investigation of different materials. Additionally, the quantitative analysis via XRF is known as a rapid and inexpensive technique with a simple sample preparation. However, deep and quantitative understanding of this defect also requires modelling to link observations with the underlying mechanisms. While traditionally XRF was limited to small areas, large area XRF mapping offers new possibilities to better quantify the extent and distribution of macrosegregation.

Numerical simulation of centreline segregation is extremely challenging due to the complex interplay between the many different phenomena [17, 18]. Flemings and Nereo [15] were among the first to model fluid flow induced by shrinkage, under several assumptions including stationary solid phase, constant but different densities for the liquid and solid, and solute partitioning via the Gulliver-Scheil equation. Many researchers then built upon their efforts. Mehrabian *et al.* [19] included intra-dendritic fluid flow during solidification using Darcy's law with flow driven by gravity. Bennon et al. [20, 21] proposed to predict macrosegregation through a continuum model based on mixture theory. Ni and Beckermann [22] developed the volume average approach, where the solute concentration is treated as a mixture of both solid and liquid phases, to rigorously account for multi-scale phenomena during solidification. Založnik and Combeau [23] developed a splitting scheme to reduce the complexity associated with coupling the two phases in order to predict macrosegregation in DC casting [24]. Nguyen et al. [25] included the movement of equiaxed grains to demonstrate the impact of solid phase transport on macrosegregation. The volume average approach is now commonly used to predict macrosegregation because it allows for the interdendritic flow induced by several mechanisms including melt flow, shrinkage, bulging, soft reduction, thermo-solutal buoyancy and the motion of equiaxed grains to be simulated.

Properly modelling macrosegregation requires heavy computational cost; the coarse mesh size and simplifications introduced to make the compute time manageable often fail to capture phenomena at the scale of the microstructure. These models are also strongly dependent on the input parameters and auxiliary models [8]. The use of simplified Level-rule, Gulliver-Scheil or Brody-Flemings microsegregation equations [26] have a significant effect on the solid evolution and thus solute concentration [8]. However, the mushy zone permeability will spatially vary due to different local liquid fraction, flow tortuosity and semisolid microstructure thus requiring a solution of fluid feeding at the microscale [19] and not simply the use of an analytical expression like Carman-Kozeny [27]. Evidence has also shown that macrosegregation cannot be accurately predicted without considering grain morphology [28]. Based on these challenges, predicting the extent of macrosegregation during continuous casting is extremely difficult. As identified by Thomas [18], it requires a comprehensive thermal/solutal model, a microsegregation model, a model for solute transport induced by shrinkage, and a model for solid deformation resulting from mechanical forces including bulging, roll misalignment, and unbending.

A better understanding of fluid flow and solute transport at both the microscopic and macroscopic levels is necessary for industry to further reduce macrosegregation during continuous casting of steel. The recent development of a mesoscale granular model of solidification, in which a representative volume element consisting of a set of equiaxed grains whereby the liquid and solid phases are independent of each other, offers new possibilities for predicting segregation in semi-solid metallic alloys [29, 30]. This granular model allows for direct consideration of the interactions between the liquid and solid while also simulating solidification [31, 32], liquid feeding [33, 34, 35] and deformation [30, 36] within a semisolid domain containing many hundreds or thousands of equiaxed grains [30]. In contrast to conventional continuum methods that are based on averaging over a representative volume element, the discrete mesh representing the geometry of individual grains and the connectivity of the liquid channels that is inherent to the mesoscale granular model of solidification allows for an accurate prediction of the relative motion between intra-dendritic flow and solid grains.

In the present study, building on our previous

mesoscale solidification and fluid flow models for steel [32, 35], a novel multiscale approach to simulating macrosegregation during continuous casting of steel is presented. This new approach directly combines heat transfer and solidification at the macroscale, fluid flow and solute transport at the scale of the mushy zone, and solute partitioning at the scale of the grains. Advection of enriched intra-dendritic liquid (i.e. mass transport due to fluid motion) resulting in macrosegregation is induced by solidification shrinkage and mechanical deformation. First, the model's ability to predict centreline segregation during continuous casting of steel is demonstrated for the case of a hypoperitectic ternary Fe-0.105C-1.55Mn (wt.%) steel. Second, the model results are compared against an experimentally-measured Mn centreline segregation profile from a steel slab commercially cast at ArcelorMittal Dofasco. Third, the effects of alloy composition, and soft reduction on the degree of segregation are explored. By combining macroscale and mesoscale modelling techniques, physical phenomena within microstructure that are classically hidden by the averaging procedure of fully continuum approaches are able to be considered. This enables new insight to be obtained on the fundamental mechanisms of centreline alloy segregation.

2. Model Description

The multi-scale and multi-physics model for predicting centreline segregation during continuous casting of steel consists of four models: (1) a 1D continuum-level macroscale heat transfer model known as CON1D [37] to obtain the temperature evolution during continuous casting, (2) a 3D mesoscale dendritic solidification [32] model, (3) a 3D mesoscale dendritic fluid flow [35] model, and (4) a 3D mesoscale solute transport and redistribution model. The four models are run sequentially (one-way coupling) using the output from the previous model, as illustrated in the flowchart shown in Fig. 1.

2.1. Macroscale Heat Transfer Model

The base input for predicting solute segregation is temperature evolution. CON1D [37] is a simple but comprehensive 1D finite-difference transient model of heat conduction during the continuous casting of steel slabs. The model domain consists of a slice of the strand thickness and length including the solidifying shell that moves down at the

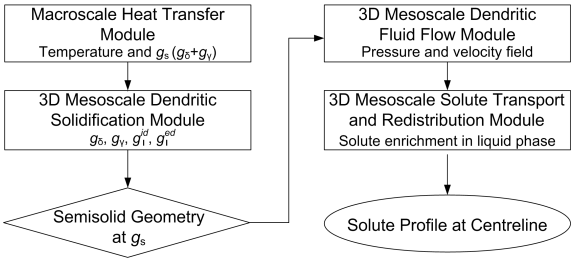

Figure 1: Flow chart outlining the sequential multi-scale one-way coupling procedure for predicting centreline segregation during continuous casting of steel. Variable definitions are provided in the text.

casting speed from the meniscus to the metallurgical length of the strand, in order to predict the temperature distribution including the shell thickness profile of the entire caster. This model takes into account many phenomena and casting parameters in the mold and spray regions including the measured mold heat flux, the amount and quality of water flow and air mist, the casting speed, the thermal properties, and the solidification path for a particular steel grade. It has been calibrated via thermocouple measurements to match several operating slab casters, including the No. 2 Continuous Caster at ArcelorMittal Dofasco in Hamilton, Canada. [38].

In calibrating the temperature evolution against the No.2CC measurements, the mold curvature, mold plating information, mold flux and steel/copper/water properties were considered. In the simulation of primary cooling, the heat flux along the mold direction was imposed for the shell thickness prediction. In the simulation of secondary cooling, The heat transfer coefficients, roll space, roll radius and contact angle, as well as nozzle spray condition and water flow rate were carefully chosen to reproduce the No.2CC production conditions. The output of CON1D simulation is the key parameter and is used as the inputs for other models shown in Fig. 1.

Fig. 2(a) shows the evolution in centreline temperature as a function of distance below the meniscus as predicted by CON1D for a commercial steel alloy with a composition of Fe-0.105C-1.55Mn (wt.%) cast at a superheat of 25°C, a speed of 0.8 m/min and having a thickness of 220 mm. Fig. 2(b) shows the corresponding lines of constant solid fraction $g_s = 0$ and $g_s = 1$ as a function of distance along the entire caster to denote the extent of the mushy zone as well as the evolving shell thickness

up to the centreline of the slab. The thermal history obtained from this macroscale simulation is used to determine the length of the mushy zone, L_m; the average cooling rate during solidification, $\dot{T}_{avg}$; and the solid fraction evolution both at the centreline, denoted P_i and 10 mm away from the centreline in the thickness direction, denoted P_{ii}. As can be seen in the figure, at the centreline $L_m \approx 2700$ mm, and $\dot{T}_{avg} \approx 0.14$°C/s.

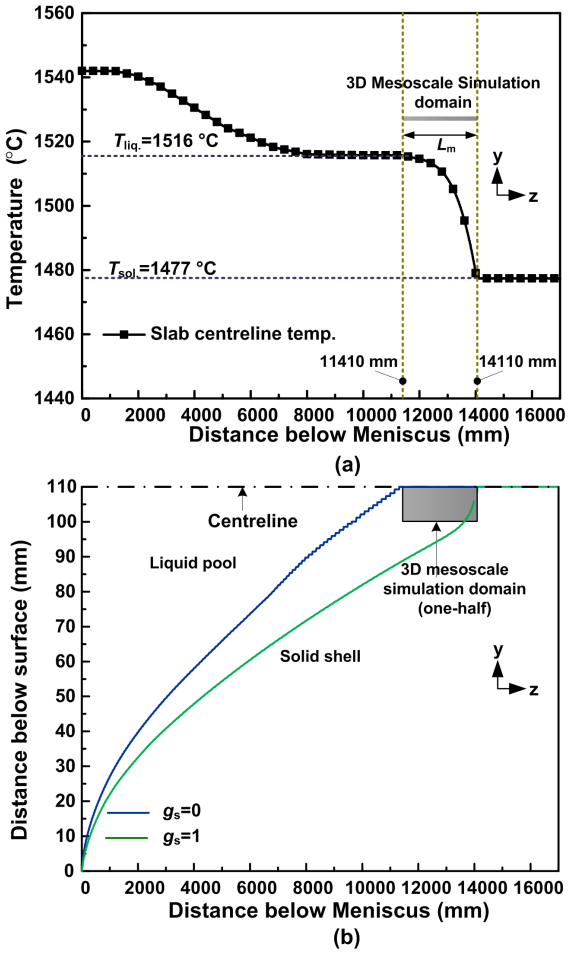

Figure 2: (a) Predicted temperature evolution along the centreline for a Fe-0.105C-1.55Mn (wt.%) slab cast at the No. 2 Continuous Casting facility at ArcelorMittal Dofasco at a speed of 0.8 m/min; (b) Corresponding lines of $g_s = 0$ and $g_s = 1$ to denote the extent of the mushy zone along the half-thickness of the caster. The grey box shows the location of the mesoscale simulation domain.

2.2. 3D Mesoscale Simulation Domain

The simulation domain of the 3D mesoscale models consists of a slice of the mushy zone near the slab centreline from the liquidus to solidus temperatures, as shown schematically in Fig. 3 (centre), as well as the grey box in Fig. 2(a). The centreline of the domain is coincident with the centreline of the slab and has dimensions of 2700 (i.e. L_m) $\times$ 20 $\times$ 20 mm^3 in the casting (z), thickness (y) and width (x) directions, respectively. Due to imposed temperatures being provided by CON1D, only temperature variations along the casting (z) and thickness (y) directions are considered; the temperature is assumed to be uniform along along the width (x) direction within each subdomain. This approximation is appropriate considering that typical slab-caster dimensions in the width dimension are on the order of ≈1000 mm while the mesoscale model is simulating only the central 20 mm.

The imposed temperatures in (z) and (y) from CON1D has been fully validated with the plant measurements, providing a real temperature variation along the casting direction. Modelling the intermediate scale between the scale of the entire process and the scale of the microstructure is obtained by having a domain large enough to include a few million grains across the complete solidification range along the centreline while discretizing separately the individual grains and the liquid channels between them.

The heavy computational cost associated with simulating such a large number of grains is overcome by partitioning the domain into 27 subdomains each 100 mm in length along z, as shown in Fig. 3 (lower). Note that the grain size is around 800 µm and thus each subdomain contains $\sim 8 \cdot 10^4$ grains. The choice of 800 µm grain size was made to match the sample used for model validation (see Section 3). The solidification, fluid flow, and solute transport models each use a different mesh within the subdomains as described in their relevant sections. Mass flux and solute flux are exchanged at the boundaries between the subdomains as a result of advection and diffusion [39]. The boundary conditions for the solidification, fluid flow, and solute transport at the inlet, outlet, lateral surfaces, and subdomain boundaries are discussed in Section 2.6.

2.3. 3D Mesoscale Dendritic Solidification Model

The 3D mesoscale dendritic solidification model [32] simulates solidification within the mesoscale simulation domain in order to create semi-solid grain structure for fluid flow and solute transport calculations.

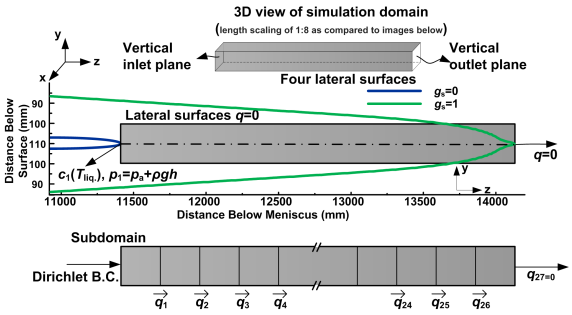

Figure 3: Schematic of the 3D mesoscale simulation domain. The centre image provides a cross-section view of the domain, showing lines of constant solid fraction $g_s = 0$ and $g_s = 1$, with colours matching Fig. 2(b). The upper and lower images show the 3D geometry and relevant boundary conditions, and division into subdomains.

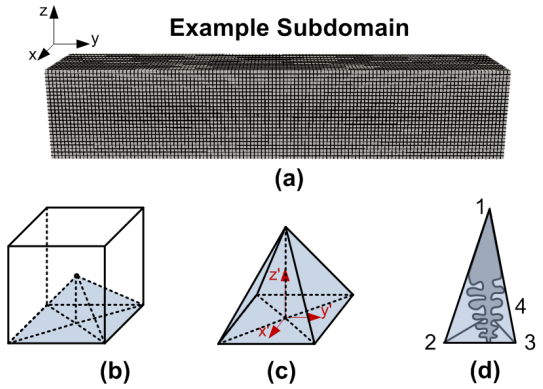

Figure 4: (a) Example subdomain, 100 x 20 x 20 mm^3 containing 78,125 cubic grains; (b) Single cube representing a grain with one of the six polyhedrons highlighted in blue; (c) Polyhedral sub-structure showing the four tetrahedral elements; and (d) A single tetrahedral element. In (d) the dendrite is shown only to illustrate equiaxed-dendritic microstructure; the dendrite tip touches the element's surface resulting in intra-dendritic liquid flow.

First, a Voronoi tessellation is applied to the simulation domain to approximate fully solidified equiaxed-dendritic grain morphology within each of the 27 rectangular subdomains. This is accomplished by placing seeds to act as grain nuclei with the density of the seeds being given by the expected final average grain size near the slab centreline. This method can be utilized to create either unstructured (random) or structured (cubic) mesh, depending on the location of the grain seeds. In our past studies [32, 35] an unstructured mesh was used to explore stochastic effects occurring right at the end of solidification. In this study, cubic grains each growing from a single classic diamond-shaped equiaxed dendritic crystal are used to further reduce computation cost. While an unstructured mesh is necessary to study defects where grain coalescence plays a major role, like hot tearing, a structured mesh efficiently reproduces the features needed to study segregation as is shown in the supplementary file S1.

Fig. 4(a) shows an example subdomain, 100x20x20 mm^3 containing 78,125 cubic grains each having an edge length of 800 µm. The edge length, equivalent to the grain size, was determined via metallography for the casting conditions shown in Fig. 2. The numerical mesh is then created by first subdividing each grain into six polyhedrons, an example of which is given in Fig. 4(b), that are each further subdivided into four tetrahedral elements as outlined by the dotted lines in Fig. 4c. For each tetrahedral element the 4 vertices are located at (1) the grain nuclei and (2,3,4) on the grain's surface as indicated in Fig. 4d. Thus, each cubic grain consists of 24 tetrahedral elements having a length of 400 µm, and each subdomain contains 1.875 million elements. Please note that the dendrite shown in Fig. 4(d) is provided only to illustrate the dendritic morphology as the mesh does not directly represent dendrites.

Second, solidification is simulated within each tetrahedral element independently of all others until a specified value of solid fraction, g_s^*, is reached as described in detail in [32, 35]. Given that the microstructure of steel is dendritic, the evolution in g_s can be predicted using a volume average approach [40, 41] as long as the alloy composition, grain size, and cooling rate are known. The main advantage of this approach is its ability to model solidification using at least three and possibly four phases (extra-dendritic liquid l^{ed}, intra-dendritic liquid l^{id}, delta-ferrite δ and austenite γ) without explicitly tracking the interfaces between the phases. Specifically, a solute mass balance is performed upon cooling to track the position of the dendrite envelope under the assumption of finite diffusion within l^{ed}, l^{id}, and δ or γ. In this way, the evolution in the volume fractions g_δ, g_γ, g_l^{id}, and g_l^{ed}, as well as the evolution in average chemical composition, can be tracked within each tetrahedral element from $g_s = 0$ to $g_s = g_s^*$. The input steel composition parameters for this volume average solidification simulation were: a grain size of 800 µm, a liquidus temperature $T_l = 1529^o$C, a cooling rate $\dot{T} = 0.14^o$C/s, an alloy composition of Fe-0.105C (wt.%), and a constant partition coeffi-

cient k_C =0.16 during initial solidification. For this composition, our CALPHAD (Thermocalc) simulations predicted an equilibrium solidification range of ≈39^{o}C, a value that was nearly identical to the one predicted by the CON1D macroscale model for Fe-0.105C-1.55 Mn (wt.%) alloy the and shown in Fig. 2.

The value of g_s^* for each tetrahedral element along the length of the mushy zone was determined and prescribed from the output of the macroscale heat transfer model. Specifically, the CON1D g_s values at P_i (centreline) and P_{ii} (10 mm away from the centreline in y) at positions corresponding to the midpoints along z of each of the 27 subdomains are extracted and then assigned as g_s^* to each tetrahedral element. This assignment is based on the (x, y, z) coordinates of the grain nuclei and using linear interpolation between the g_s values for P_i and P_{ii}. Fig. 5 compares the CON1D-output g_s values at both P_i and P_{ii} with the mesoscale model g_s profiles resulting from having imposed g_s^* on each tetrahedral element. As expected, an excellent match is achieved. The "stair-case" effect seen in z in the mesoscale curves is because it has been it has been assumed that g_s^* remains constant along z and x within each subdomain, and only varies in y. Please note that the solid fraction near the centreline is initially greater than zero since the upstream fully-liquid pool is expected to have little effect on the centreline segregation phenomena of interest; P_{ii} solidifies before P_i. Note also that since P_{ii} = 1 in each of subdomains 21-27, the solidus line falls within the subdomain and moves closer towards the centre with increasing distance below the meniscus (increasing subdomain number).

2.4. 3D Mesoscale Dendritic Fluid Flow Model

The 3D mesoscale dendritic fluid flow model [35] calculates the pressure and fluid velocity distribution resulting from solidification shrinkage and mechanical deformation throughout the 27 subdomains of the semi-solid mesoscale simulation domain. The mesh consists of a set of fluid flow elements, each consisting of a pair of solidification model tetrahedral elements from two adjacent grains as shown in Fig. 2 of [35].

In our previous study [35], both intra-dendritic and extra-dendritic flow were considered. The region enclosed by the dendrite envelope was treated as a uniform porous medium [42] with an internal liquid fraction to simulate intra-dendritic flow. The region outside the dendrite envelope but still within

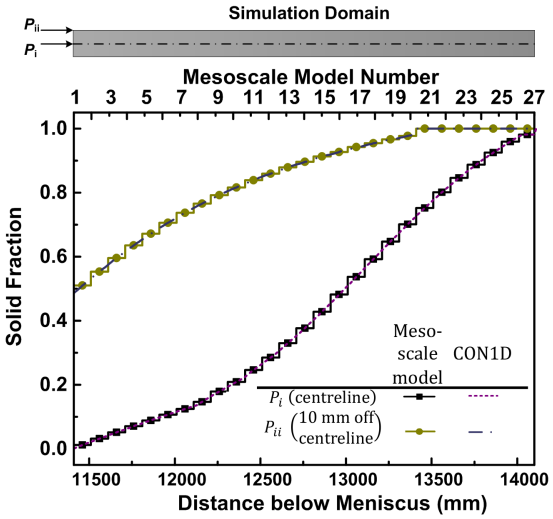

Figure 5: g_s variation at positions P_i (centreline) and P_{ii} (10 mm away from the centreline in the thickness direction), along with a schematic of the applied subdivision used to reduce computation time. Note that the solid fraction is a sum of both δ and γ.

the tetrahedral element was treated as a fully liquid channel. In the limit where the dendrite tips touch then all the remaining liquid is intra-dendritic, as shown in Fig. 4, and the whole structure behaves as a porous medium with a characteristic length scale given by the secondary dendrite arm spacing. In the present study, only the case of intra-dendritic flow is considered. This is justified by the assumptions that: (1) at a final grain size as large as ∼800 µm the microstructure is fully equiaxed-dendritic even at low solid fraction, and (2) the phenomena leading to centerline segregation essentially occur in the part of the mushy zone where the equiaxed dendrites are packed, *i.e.*, the dendrite envelopes touch and thus all remaining liquid is intra-dendritic. For the solidification conditions prescribed by CON1D, the 3D mesoscale dendritic solidification model predicts that the dendrite envelopes touch at $g_s = 0.3$. Further, the flow is assumed to be quasi-steady state, irrotational and flowing in a direction that is parallel to the triangular facet made where the two facing tetrahedral elements meet.

In a frame of reference moving at the casting speed, and neglecting gravity as well as flow in the strand width direction, the intra-dendritic fluid velocity can be expressed as

$$-\nabla p - \frac{\mu_l}{K\left(g_l\right)}(\vec{v}_l g_l) = 0, \qquad (1)$$

where μ_l represents the dynamic viscosity, p is the gauge pressure, $\vec{v}_l$ is the intrinsic average liquid velocity, g_l is the fraction liquid, and $K(g_l)$ is the local permeability within the dendrite envelope (calculated with the Carman-Kozeny equation [27]). This expression is equivalent to Eqs. 1 and 2 of [35] assuming that $g_l^{ed} = 0$.

By conducting a mass balance over the fluid flow element and assuming liquid incompressibility ($\nabla \cdot \vec{v}_l = 0$) the pressure within the mushy zone can be determined from

$$\int_{S_l^e} \left(-\frac{K(g_l)}{\mu_l} \right) \nabla p \cdot \vec{n} dS - v^* \beta S_{sl}^e + \Delta v_{liq} = 0, \quad (2)$$

where S_l^e represents the total surface area of a fluid flow element, i.e. the six remaining sides of the two facing tetrahedral elements, S_{sl}^e is the solid/liquid interfacial area assuming partitioning between the solid and liquid phases, v^* is the δ/liquid or γ/liquid interface velocity at the scale of a tetrahedral element predicted by the dendritic solidification model, $\beta = (\rho_s/\rho_l - 1)$ is the shrinkage factor with ρ_s and ρ_l representing the average solid (δ and γ) and liquid densities. Δv_{liq} is the increase in volumetric flow rate that is required to compensate for mechanical deformation at the scale of an individual element, and is given as

$$\Delta v_{liq} = \frac{\dot{\varepsilon}_{sv}}{(1 - g_s)} * V_{liq}, \quad (3)$$

where $\dot{\varepsilon}_{sv}$ is the volumetric part of the strain rate tensor applied on the domain, and calculated via $\dot{\varepsilon}_{sv} = \dot{\varepsilon}_{xx} + \dot{\varepsilon}_{yy} + \dot{\varepsilon}_{zz}$, and V_{liq} represents the volume of liquid present in an element. Note that while Eq. 3 can be used to represent the effects of mechanical deformation on fluid flow in the semi-solid domain of the current model, mechanical deformation itself is not directly simulated. Flow due to buoyancy is not considered. Furthermore, it is assumed that the solid velocity equals the casting speed, and thus in the moving frame of reference it would have a relative velocity of zero and can be neglected.

2.5. 3D Mesoscale Solute Transport Model

The 3D mesoscale steady-state solute transport and redistribution model predicts solute distribution within the mesoscale simulation domain's liquid channels due to advection and diffusion resulting from solidification shrinkage and mechanical deformation. This problem is solved by considering solute mass balances in the solid and liquid phases, and solute transport in the liquid phase, using as inputs the semi-solid grain structure from the dendritic solidification model and the liquid velocity and pressure fields from the dendritic fluid flow model.

The averaged mass balance equations in the solid and liquid phases at steady state during solidification, as well as at the solid/liquid interface, can be written as

$$\rho_s \nabla \cdot (g_s \vec{v}_s) = \rho_s S_v \bar{v}_s^*, \quad (4)$$

$$\rho_l \nabla \cdot (g_l \vec{v}_l) = \rho_l S_v \bar{v}_l^*, \quad (5)$$

$$\rho_s S_v \bar{v}_s^* + \rho_l S_v \bar{v}_l^* = 0. \quad (6)$$

where $g_s = 1 - g_l$ is the volume fraction of the solid, S_v is the interfacial area concentration, $\vec{v}_s$ and $\vec{v}_l$ are the intrinsic average solid and liquid velocities, and $\bar{v}_s^*$ and $\bar{v}_l^*$ is the average velocity of the solid-liquid interface, relative to the velocity of the solid and liquid phase, respectively.

By combining Eqs. 5 to 6, the mass balance for the liquid phase can be simplified to

$$\nabla \cdot (g_l \vec{v}_l) = -\frac{\rho_s}{\rho_l} S_v \bar{v}_s^*. \quad (7)$$

The solute conservation equation in the liquid phase at steady state during solidification, as well as at solid/liquid interface, can thus be written as

$$\rho_l \nabla \cdot (g_l c_l \vec{v}_l) - \rho_l D_l \nabla \cdot (g_l \nabla c_l) = \rho_l S_v \bar{v}_l^* c_l^* + \rho_l D_l S_v \cdot \left(\frac{\partial c_l}{\partial n} \right)^*, \quad (8)$$

$$\rho_s S_v \bar{v}_s^* c_s^* = -\rho_l S_v \bar{v}_l^* c_l^* - \rho_l D_l S_v \cdot \left(\frac{\partial c_l}{\partial n} \right)^*. \quad (9)$$

assuming no diffusion in the solid phase. In these equations, c_l, c_s represent the intrinsic solute concentrations in the liquid and solid phases, respectively, c_s^* and c_l^* represent the equilibrium solute concentrations in the solid and in the liquid at the solid-liquid interface, D_l represents the diffusion coefficient of the solute in liquid phase, and $\left(\frac{\partial c_l}{\partial n}\right)^*$ denotes the concentration gradient in the liquid at the interface.

Then, by combining Eqs. 8 and 9, the solute conservation equation in the liquid phase is simplified to

$$\rho_l c_l \nabla \cdot (g_l \vec{v}_l) + \rho_l g_l \vec{v}_l \cdot \nabla c_l - \rho_l D_l \nabla \cdot (g_l \nabla c_l) = -\rho_s S_v \bar{v}_s^* c_s^*, \quad (10)$$

where the RHS term represents the solute trapped by solidification, and LHS terms represent solute transport due to advection, interface motion, and diffusion. Finally, to simulate solute transport through the liquid phase within the mushy zone, Eq. 10 is rearranged, and its first term replaced with Eq. 7 to give

$$\vec{v}_l \cdot \nabla c_l - \frac{D_l}{g_l} \nabla \cdot (g_l \nabla c_l) = \frac{\rho_s}{\rho_l} \frac{S_v}{g_l} \vec{v}_s^* \left(c_l - c_s^*\right), \quad (11)$$

where c_s^* is can be obtained by $c_s^* = c_l^* \cdot k$ and k is the partition coefficient.

Please note that although the 3D mesoscale dendritic solidification model uses a binary Fe-C alloy to create the semisolid structure, the solute transport model contains no such limitation. In principle, the model could be applied to simulate transport for any number of solute elements in this steel grade assuming no cross-diffusion terms in the diffusion matrix. Here it is applied to Mn diffusion and segregation. All that is needed are the fraction-solid-dependent values of c_l^* and k for the elements of interest. For this study, these values were determined from Thermocalc (Database TCFE 11) for the composition Fe-0.105C-1.55Mn (wt.%) ternary system.

2.6. Numerical Implementation

The four models described above are solved sequentially. First, the macroscale heat transfer model (CON1D) is run to obtain the needed temperature and phase fraction profiles to create the mesoscale simulation domain. Second, the 3D dendritic solidification model is applied to each subdomain to create 3D semi-solid geometry containing the average phase fractions (δ, γ and L) and temperatures for that region from CON1D. Third, the 3D dendritic fluid flow model is applied [32] to the entire mesoscale simulation domain to calculate the overall pressure distribution and the average fluid velocity within each element. Finally, the solute transport model is applied to acquire the solute distribution map within the semi-solid structure of grains and liquid channels. CON1D is written in FORTRAN and run as a standalone simulation; the mesoscale models are written in C++ and run sequentially as one single simulation.

The fluid flow simulation is solved over the entire domain using a two-stage coupling process to determine the unknown fluid pressures and velocities at the subdomain boundaries neglecting the influence of casting speed. The boundary conditions (Fig. 3) consist of a constant pressure p_1 on the inlet surface, zero mass flux on the lateral surfaces as lateral feeding is assumed to be zero, and zero mass flux on the outlet surface as liquid mass cannot flow through the solidified boundary. The first half of this two-stage process starts with the subdomain nearest the solidus, S_{27} with q_{27}=0 kg/(m^{2}s) applied to the outlet surface. From the results of this subdomain simulation, the fluid velocity $\vec{v}_{l,26}$ on the inlet side of S_{27} is determined.

Then, a similar step is applied to S_{26} using $q_{26} = \rho_l g_l \vec{v}_{l,26}$ to calculate the unknown $\vec{v}_{l,25}$ After 27 simulations, q_1 between S_1 and S_2 is obtained. The second half of the coupling process starts by solving S_1 for the known pressure p_1 on the inlet surface, known q_1 on the right side from the first half of the simulation, and closed lateral surfaces. From this, the pressure distribution within S_1 as well as p_2 at the interface between S_1 and S_2 are obtained. This process continues until the pressure distribution through all subdomains is determined.

With knowledge of the velocity fields throughout the 3D mesoscale simulation domain, the solute field is determined beginning at the inlet surface between S_1 and the melt pool, and terminating at S_{27} following the same procedure as outlined above. The boundary conditions consist of a constant solute concentration c_1 on the inlet surface adjacent to the melt pool equal to the nominal alloy composition, and zero solute flux on the lateral and outlet surfaces. The final composition profile at the outlet of subdomain S_{27} can be compared with the measured composition profile across the strand thickness.

The fluid flow and solute transport equations within an individual subdomain are solved as follows. First, on a single fluid flow element the intradendritic liquid channel is divided into 1000 segments aligned in a direction perpenticular to the triangular facet made where the two facing tetrahedral elements meet.

Then the integration of Eq. 2 is computed numerically. By applying Green's theorem, one obtains the coefficient of the Laplacian of the pressure field, $\nabla^2 p$. The 3D fluid flow element is then simplified to a 3-node 2D triangular element having coordinates as nodes (2,3,4) shown in Fig. 4 by using the assumption of parallel flow. The resulting elemental pressure field is given by

$$p_e = N_i p_i, \; i = 1..3. \quad (12)$$

where p_i represents the nodal pressures, N_i represents the shape functions of the triangular element that approximate the pressure field within a fluid flow element in the local x', y', z' coordinate system shown in Fig. 4(c) that is parallel to and located at the centre of the triangular facet made where the two facing tetrahedral elements meet. Applying the Galerkin finite element method to Eq. 2, the elemental matrix equation for the fluid flow problem and the resulting global stiffness matrix are assembled and then solved with a conjugate gradient linear iterative method as fully described in [35].

With the pressure known, the components of $\vec{v}^{id}$ are determined for each fluid flow element via Eq. 1 as

$$\vec{v}_{x'} = -\frac{K\left(g_l\right)}{\mu g_l}\left(\frac{\partial(N_i \cdot p_i)}{\partial x'}\right), \; i = 1..3, \tag{13}$$

$$\vec{v}_{y'} = -\frac{K\left(g_l\right)}{\mu g_l}\left(\frac{\partial(N_i \cdot p_i)}{\partial y'}\right), \; i = 1..3. \tag{14}$$

The use of a 3-node 2D triangular element to approximate the pressure field, Eq. 12, obviously results in a zero pressure gradient and thus zero flow in z', i.e. $\vec{v}^{id}_{z'} = 0$.

For the solute transport problem, integration of Eq. 11 on a single element is computed in a similar manner to the fluid flow problem. Assuming once again that the mesh can be simplified to 2D triangular elements, the solute concentrations in the liquid are mapped to nodal concentrations c_{li} as

$$c_e = N_i c_{li}, \; i = 1..3. \tag{15}$$

Then, by applying the Galerkin finite element method to Eq. 11, the elemental matrix equation for the solute transport problem is obtained,

$$[M]^e \begin{Bmatrix} c_{l1} \\ c_{l2} \\ c_{l3} \end{Bmatrix} = b^e + \{\phi\}^e, \tag{16}$$

$$[M]^e_{ij} = \int_\Omega N_i \vec{v}_{lx'} \frac{\partial N_j}{\partial x'} + N_i \vec{v}_{ly'} \frac{\partial N_j}{\partial y'} + D \frac{\partial N_i}{\partial x'} \frac{\partial N_j}{\partial x'} + D \frac{\partial N_i}{\partial y'} \frac{\partial N_j}{\partial y'} - \frac{\rho_s}{\rho_l} \frac{S_v}{g'_l} \vec{v}^*_s N_i N_j dS, \tag{17}$$

$$\{b\}^e_i = \int_\Omega -N_i \frac{\rho_s}{\rho_l} \frac{S_v}{g'_l} \vec{v}^*_s dS, \tag{18}$$

$$\{\phi\}^e_{ij} = \int_{\partial\Omega} N_i q^s dS, \tag{19}$$

where $[M]^e$ is the element stiffness matrix, b^e is the load vector, $\{\phi\}^e$ is the imposed boundary condition, and q is the solute flux at the element boundaries.

Once the element matrices have been developed, they are assembled together into a global stiffness matrix (for an individual subdomain), and then solved using a general minimal residual method via the C++ open access library IML++ [43]. Because of this assembly, the solute fluxes q^s remain only on the external boundary of the simulation domain and the interfaces between subdomains. The general minimal residual method has been utilized for the solute transport problem since the presence of the fluid velocity in the first term of Eq. (11) results in $[M]^e$ being unsymmetric.

Computational expenses and CPU time for simulations are among the main concerns limiting use of numerical models, especially computationally-intensive multi-physics models such as the macrosegregation in continuous-casting of steel [44]. One of the advantages of the present mesoscale model is its efficient performance. The total time to simulate centreline segregation using the approach described above including 50 million computational cells, using a Linux machine with a 3.00 GHz 2-core processor, is on the order of 8 hours. In contrast, the use of a continuum model for such a simulation would be cost prohibitive.

3. Experimental Measurements

In order to validate the new multi-scale alloy segregation model, a large (90x90 mm^2) composition map of Mn at a resolution of 250 µm was acquired from a polished steel sample via X-ray fluorescence (XRF) using a bespoke instrument at ArcelorMittal's Global Research and Development Hamilton [45, 46]. The sample, oriented parallel to the casting direction, was taken from the centreline of a steel slab as shown in Fig. 6 and then prepared for XRF using standard metallographic procedures. The slab, of composition ≈ Fe-0.105C-1.55Mn (wt.%) was continuously cast at the No.2 Continuous Caster at ArcelorMittal Dofasco in Hamilton, Canada at a casting speed of 0.8 m/min with a thickness of 220 mm and a width of 1500 mm. Metallography performed on a slab sample cast under these conditions determined that the centreline consisted of equiaxed grains, with an average grain size of ≈800 µm.

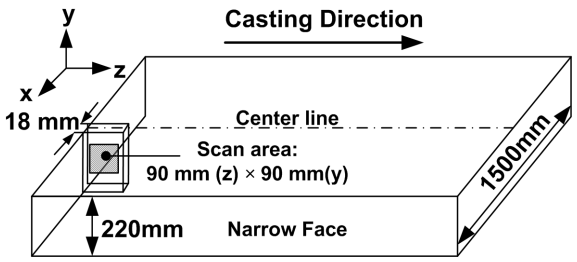

Figure 6: Schematic showing the orientation and size of the steel sample used for large-scale XRF measurementation.

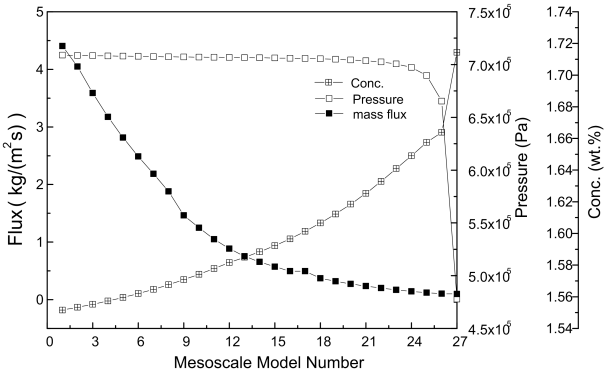

Figure 7: Predicted variation in pressure, liquid flux, and average Mn concentration in each mesoscale simulation subdomain. $\bar{c}_l$ represents the average c_l across all the liquid channels at the subdomain interfaces.

4. Results and Discussion

In the following sections, the mesoscale solute transport model is applied to the entire mushy zone of the casting slab to investigate the centreline segregation of Mn in a Fe-0.105C-1.55Mn (wt.%) ternary system followed by parametric studies. First, the solute flow predictions and centreline segregation during continuous casting are examined and are compared to the experimental data. Then, results are presented to conduct a preliminary investigation of the effect of alloy content, and soft reduction on centreline segregation of Mn.

4.1. Model Predictions

Fig. 7 shows the pressure variation (p), liquid flux (q), and average Mn concentration variation in the liquid ($\bar{c}_l$) throughout the mushy zone as predicted by the 3D mesoscale fluid flow and solute transport models during continuous casting of steel, for the macroscale thermal conditions as given in Fig. 2. The alloy composition on the inlet side of the first subdomain, Fig. 3, is fixed to a value of 1.55 wt.% Mn.

As can be seen, the pressure decreases only slightly during the first 25 subdomains, whereas it drops significantly in the last two subdomains due to the low permeability near the solidus. The corresponding liquid flux is shown to decrease incrementally until it reaches zero at the solidus line. The average Mn concentration in the liquid phase also progressively accumulates throughout the mesoscale simulation domain, due to solute partitioning between the solid and liquid phases as well as fluid flow from one region of the mushy zone to another.

Fig. 8 shows the corresponding Mn solute contours within four subdomains (S_1, S_{20}, S_{26}, and S_{27}) that range from very low to very high solid fraction. Images (a),(b), and (c) use one colour map, while image (d) uses another. The coordinates of each subdomain with reference to the casting length (2) are also plotted for the purposes of identifying its location. During the initial solidification, S_1 (Fig. 8(a)), the solute profile is largely uniform, with a small build-up of Mn towards the centreline. Further down the caster, S_{20} (Fig. 8(b)), the flow is likely to compensate for more of the shrinkage in the transverse direction and thus solute becomes enriched transverse to z. Once the solidus line reaches 10 mm away from the centreline, the fluid is not able to carry the solute away due to the solidified sidewalls. In S_{26} (Fig. 8(c)), the solidus line is already within the subdomain and thus enrichment in the transverse direction as well as near the bottom of the subdomain is occurring. Finally, the enrichment of solute near the centre of the casting slab is captured in Fig. 8(d) at the last stages of solidification when only the centre remains. Comparing Figs. 8(a)-(d), the presence of fluid flow and solute partitioning lead eventually to the enrichment of solute within liquid channels inside the solid structure indicated as by the colour bars.

The curved contours that can be seen towards the lower end of each subdomain and most visible in Fig. 8(b) can be attributed to the fluid flow boundary conditions on each subdomain, since a zero mass flux is imposed on the four lateral interfaces while a finite flux is imposed on the interface between subdomains. Given this set of boundary conditions, the outflow condition may not match exactly with the inflow condition of the next subdomain. However this small error should not be overemphasized

as most of the solute enrichment within the mushy zone occurs in the last subdomain where all the interfaces except for the inlet have been closed (zero mass flux) as they have reached a solid fraction of one.

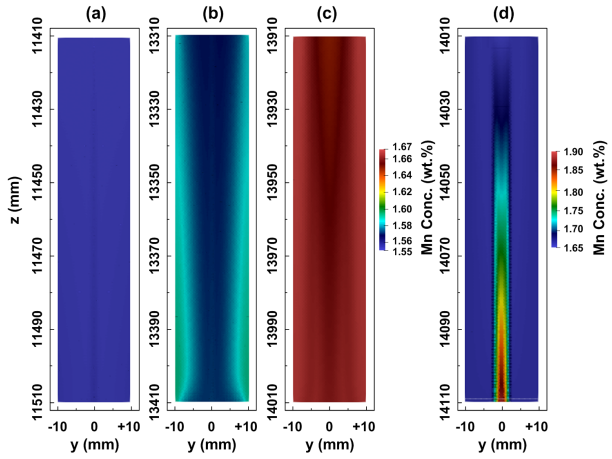

Figure 8: Contour plots of solute distribution calculated in ((a)-(d)) subdomains S_1, S_{20}, S_{26}, and S_{27}.

4.2. Model Validation

The large-scale composition map shown in Fig. 9, providing the distribution of Mn near the centreline of a continuously-cast steel slab with composition Fe-0.105C-1.55Mn (wt.%), was used for model validation. The image (a) provides the full area-map distribution while (b) shows the detail across an arbitrarily-placed line perpendicular to the centreline. As can be seen, the acquired solute map reveals clearly the occurrence of solute enrichment in Mn especially towards the centreline of the slab. Note that in this section, both the measured and simulated Mn compositions have been normalized in the same way - by subtracting the minimum measured value and dividing by the difference between the maximum and minimum measured values (rounded to the nearest 0.1wt.%).

Solidification morphology: The dendritic structure is illustrated by the Mn-poor areas, while the inter-dendritic region with segregated Mn is represented by the Mn-rich areas. Based on the location of Mn enrichment, columnar dendrites can be inferred to grow parallel along the heat flux direction from the surface towards the centre, but then become blocked by the equiaxed dendrites forming near the centre (≈20 mm -wide through the centreline). There is also a region of random equiaxed grains on the right side of map due to the sedimentation during the casting process.

Solute enrichment: The solute is seen to be enriched near the centre of the test sample where $y = 0$, i.e. the centre of the as-cast slab. Referring now to the solute profile over the arbitrary-placed line, solute inhomogeneity is easily identified by the peaks and valleys in Mn content. The highest is observed near the centre corresponding to the slightly red region in Fig. 9(a). The valleys correspond approximately to the centre of the solid dendrites and perhaps the centre of secondary dendrite arms, while the peaks correspond approximately to final solidified liquid.

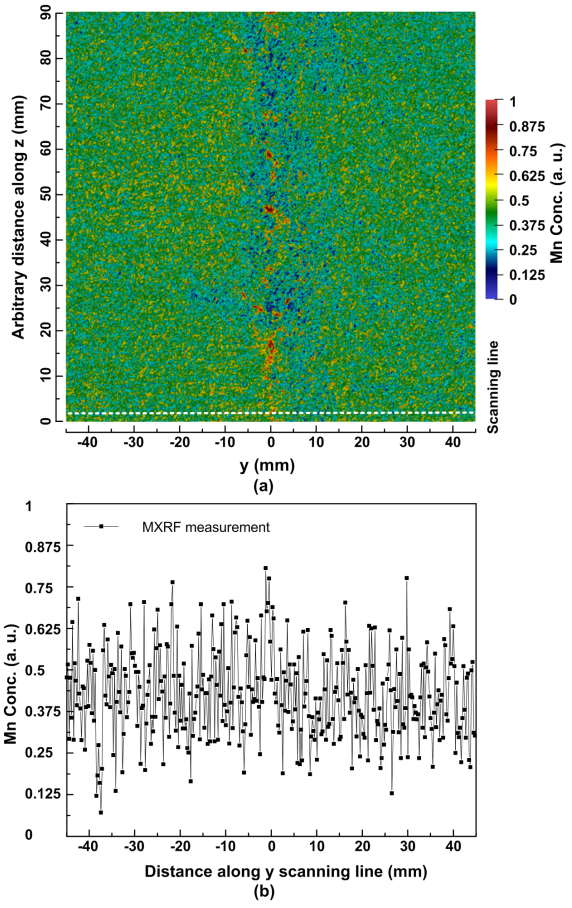

Figure 9: XRF (a) Mn large-scale solute map and (b) detail across an arbitrarily-placed line through the centreline of a continuously-cast slab. The casting direction is vertical, pointing upwards.

The model validation, Fig. 10, is carried out by comparing the measured Mn content along the arbitrarily-placed line against the simulation results. In this figure, the blue triangles represent the

predicted solute concentration within the discrete liquid channels at the end of solidification while the black line and small black squares represent the MXRF measurements. As can be seen, excellent agreement is achieved with the peak at the centreline, and is still a good fit up to 8 mm away from the center. The simulation is able to reproduce only the peaks in the measured data, and not the valleys. This is because the simulation only accounts for solute redistribution in the discrete liquid channels at the end of solidification (i.e. the outlet of subdomain 27) and does not output the composition of the solid phase. The experimental data shows the final solidified liquid as peaks and initially solidified dendrites as valleys. Please note that in the experimental data the Mn concentration was acquired at a step size of 0.25 mm and a spot size<<step size [45, 46] thus the link between microstructure and Mn segregation is only approximate. Note also that the simulation data is for $g_s = 0.981$ at the centre since only solute transport within the liquid is included.

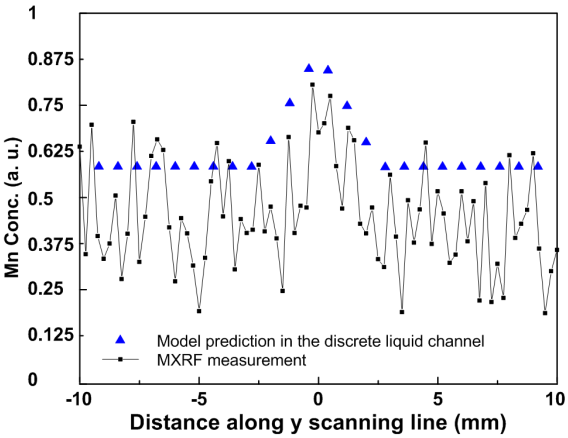

Figure 10: Comparison of solute distribution via MXRF measurement and 3D mesoscale model along the central 20 mm of the casting. The casting direction is vertical, pointing upwards.

4.3. Parametric Studies Examining Centreline Segregation

Having validated the multi-scale, multi-physics model, it is now possible to investigate how centreline segregation varies for different alloy compositions, and processing conditions (soft reduction). For this work, a set of simulations were carried out assuming the same set of conditions as the simulations presented in Section 4.1.

4.3.1. Effect of Alloy Composition

The relative severity of macrosegregation for different steels is critically important when industry is designing new grades, especially for advanced high strength steels. Mechanistically, it is the presence of a peritectic transformation in the AHSS grades that influences greatly the segregation due to the corresponding changes in solidification shrinkage which change the interdendritic flow pattern. Fig. 11 thus shows solute maps predicted for (a) a hypo-peritectic (Fe-0.105wt.%C-1.55wt.%Mn) and (b) a non-peritectic (Fe-0.05wt.%C-1.55wt.%Mn) alloy. As can be seen in this figure, centreline segregation is considerably more severe in a hypo-peritectic grade as compared with a non-peritectic grade. The quantitative comparison along the dashed line located at 5 mm away from the solidus line perpendicular to z direction is shown in Fig. 11(c). Near the center, the peak is quite high for the hypo-peritectic grade while the solute localization within the non-peritectic grade is relatively even. The higher concentration is attributed to two reasons. First, the shrinkage caused by the peritectic transformation near the center requires more liquid to compensate the volume change; the arriving liquid is solute-rich. Second, the solute rejected from the solid phase per unit time will increase due to the higher growth rate of the γ phase.

4.3.2. Effect of Soft Reduction

Soft reduction is a method whereby a small amount of deformation is applied during continuous casting by careful decrease in the distance between successive support rolls, in caster segments just before the point of final solidification. This deformation is intended to match the liquid shrinkage in order to lessen fluid flow which is responsible for macrosegregation in the solidified product. The amount of soft reduction applied during the process is usually quantified as a deformation distance per unit length of shell surface down the caster with units of mm/m and termed Equivalent Soft Reduction (ESR). A typical industrial value for ESR is 1 mm/m.

Our new multi-scale and multi-physics model is able to take into account the effects of soft reduction through the Δv_{liq} term of Eq. 2 and correspondingly $\dot{\varepsilon}_{sv}$ in Eq. 3. Numerically, this can be introduced as

$$\dot{\varepsilon}_{sv} = \mathrm{ESR} \cdot \frac{v}{t}, \tag{20}$$

where v is the casting speed and t is the thickness of the slab. The underlying assumption is that deformation is localized to the liquid phase and also occurs uniformly for every grain within a subdomain experiencing ESR.

Fig. 12 shows solute maps for subdomain S_{27} experiencing ESR values of -1.3, +2.7, and +6.75 mm/m, along with a base case having no soft reduction. Negative values of ESR represent compression of the semi-solid slab, i.e. traditional soft reduction, while positive value represent tension e.g. due to incorrect machine taper or bulging that could lead to opening of the liquid channels.

As can be seen in the figure, the application of -1.3 mm/min of ESR, image (b), shows a thinner centrally segregated region with a lower maximum value along the dashed line 5 mm away from the solidus as compared to the base case of 0 ESR, image (a). This appears to have been accomplished by squeezing some of the segregated liquid upstream, which would then redistribute in the thickness direction prior to final solidification. When +2.7 mm/m of ESR is applied, image (c), i.e. a moderate amount of tension, the final segregated region is wider and appears to be greater in average concentration than either (a) or (b). This is consistent with what is known from plant measurements and is a result of sucking enriched liquid from upstream to the point of final solidification. Finally, the case of +6.75 mm/m of ESR, image (d), shows an extreme case of tensile slab deformation. Although the maximum concentration is less, the segregated region is certainly very wide and the total amount of segregated solute is larger, so this situation would likely lead to quality issues.

A key advantage of the current methodology over previous studies is the computational cost; parametric studies can be easily conducted to determine the effects of process parameters on segregation patterns.

5. Conclusions

A 3D solute transport model consisting of: (1) a 1D macroscale heat transfer and solidification model, (2) a 3D mesoscale dendritic solidification model, (3) a 3D mesoscale dendritic fluid flow model, and (4) a 3D mesoscale solute transport and redistribution model has been developed to quantitatively predict the solute redistribution induced by the solidification shrinkage and mechanical deformation. This model is built on the formulation of continuum equations and simulates the important physical phenomena associated with macrosegregation formation during solidification processing of steel. This new technique captures the semi-solid grain morphology during solidification, the complex tortuosity of flows around the inter-dendritic liquid channels, solute partitioning at the scale of the microstructure, and solute transport at a scale of continuous casting. Using this approach enables consideration of physical phenomena among different phases that have traditionally been hidden when using averaging volume techniques. The enrichment of solute within thin liquid channels predicted by the 3D solute transport model has been validated with the measurements via MXRF quantitatively. Thus, the current model provides an alternative to conventional continuum-level solute transport models that requires heavy computational cost.

The results of our simulations have revealed new insight into the underlying mechanisms causing centerline segregation:

- Solute partitioning combined with intra-dendritic fluid flow leads eventually to liquid channels enriched with solute. The solute concentration in the intra-dendritic liquid near a casting's centerline gradually increases during solidification, and sharply increases near the end;
- Centreline segregation is more severe in a hypo-peritectic grade compared with non-peritectic due to solidification shrinkage and the higher growth rate of the austenite phase; and
- The change in flow behaviour in response to deformation changes the solute distribution as centreline segregation is reduced with an increase of compression strain rate (such as caused by soft reduction) but increases with the application of tensile strain rate (such as caused by bulding).

Acknowledgements

The authors wish to thank the Natural Sciences and Engineering Research Council of Canada (NSERC) and the McMaster Steel Research Centre for financial support.

Declaration of Competing Interests

The authors declare that they have no known competing financial interests or personal relation-

ships that could have appeared to influence the work reported in this paper.

References

[1] W. Kurz, D. J. Fisher, Fundamentals of Solidification, Trans Tech Publications, Aedermannsdorf, Switzerland, 1998.

[2] F. Mayer, M. Wu, A. Ludwig, On the formation of centreline segregation in continuous slab casting of steel due to bulging and/or feeding, steel research international 81 (8) (2010) 660–667.

[3] Y.-M. Won, B. G. Thomas, Simple model of microsegregation during solidification of steels, Metallurgical and Materials Transactions A 32 (7) (2001) 1755–1767.

[4] M. El-Bealy, On the mechanism of halfwaycracks and macro-segregation in continuously cast steel slabs. i: Halfway cracks, Scandinavian Journal of Metallurgy 24 (2) (1995) 63–80.

[5] H. MIZUKAMI, M. KOMATSU, T. KITAGAWA, K. KAWAKAMI, Effect of electromagnetic stirring at the final stage of solidification of continuously cast strand, Tetsu-to-Hagané 70 (2) (1984) 194–200.

[6] S. Choudhary, S. Ganguly, Morphology and segregation in continuously cast high carbon steel billets, ISIJ International 47 (12) (2007) 1759–1766.

[7] V. Ludlow, A. Normanton, A. Anderson, M. Thiele, J. Ciriza, J. Laraudogoitia, W. Van Der Knoop, Strategy to minimise central segregation in high carbon steel grades during billet casting, Ironmaking & steelmaking 32 (1) (2005) 68–74.

[8] E. J. Pickering, Macrosegregation in steel ingots: The applicability of modelling and characterisation techniques, ISIJ International 53 (6) (2013) 935–949.

[9] N. Yoshida, O. Umezawa, K. Nagai, Influence of phosphorus on solidification structure in continuously cast 0.1 mass% carbon steel, ISIJ International 43 (3) (2003) 348–357.

[10] T. Brune, K. Kortzak, D. Senk, N. Reuther, M. Schäperkötter, A three dimensional model to characterize the centerline segregation in cc slabs, steel research international 86 (1) (2015) 33–39.

[11] H. Preßlinger, S. Ilie, P. Reisinger, A. Schiefermüller, A. Pissenberger, E. Parteder, C. Bernhard, Methods for assessment of slab centre segregation as a tool to control slab continuous casting with soft reduction, ISIJ International 46 (12) (2006) 1845–1851.

[12] D. G. Eskin, J. Zuidema Jr., V. I. Savran, L. Katgerman, Structure Formation and Macrosegregation under Different Process Conditions during DC Casting, Materials Science and Engineering A 384 (2004) 232–244.

[13] S. Choudhary, S. Ganguly, A. Sengupta, V. Sharma, Solidification morphology and segregation in continuously cast steel slab, Journal of Materials Processing Technology 243 (2017) 312–321.

[14] T. Koshikawa, M. Bellet, C.-A. Gandin, H. Yamamura, M. Bobadilla, Experimental study and two-phase numerical modeling of macrosegregation induced by solid deformation during punch pressing of solidifying steel ingots, Acta Materialia 124 (2017) 513–527.

[15] M. C. Flemings, G. Nereo, Macrosegregation. pt. 1, AIME Met Soc Trans 239 (9) (1967) 1449–1461.

[16] E. J. Pickering, C. Chesman, S. Al-Bermani, M. Holland, P. Davies, J. Talamantes-Silva, A comprehensive case study of macrosegregation in a steel ingot, Metallurgical and Materials Transactions B 46 (4) (2015) 1860–1874.

[17] T. Kajatani, J.-M. Drezet, M. Rappaz, Numerical simulation of deformation-induced segregation in continuous casting of steel, Metallurgical and Materials Transactions A 32 (6) (2001) 1479–1491.

[18] B. G. Thomas, Review on modeling and simulation of continuous casting, steel research international 89 (1) (2018) 1700312.

[19] R. Mehrabian, M. Keane, M. Flemings, Interdendritic fluid flow and macrosegregation; influence of gravity, Metallurgical and Materials Transactions B 1 (5) (1970) 1209–1220.

[20] W. Bennon, F. Incropera, A continuum model for momentum, heat and species transport in binary solid-liquid phase change systems—i. model formulation, International Journal of Heat and Mass Transfer 30 (10) (1987) 2161–2170.

[21] W. Bennon, F. Incropera, A continuum model for momentum, heat and species transport in binary solid-liquid phase change systems—ii. application to solidification in a rectangular cavity, International Journal of Heat and Mass Transfer 30 (10) (1987) 2171–2187.

[22] J. Ni, C. Beckermann, A volume-averaged two-phase model for transport phenomena during solidification, Metallurgical Transactions B 22B (1991) 349–361.

[23] M. Založnik, H. Combeau, An operator splitting scheme for coupling macroscopic transport and grain growth in a two-phase multiscale solidification model: Part i–model and solution scheme, Computational Materials Science 48 (1) (2010) 1–10.

[24] M. Založnik, A. Kumar, H. Combeau, M. Bedel, P. Jarry, E. Waz, Influence of transport mechanisms on macrosegregation formation in direct chill cast industrial scale aluminum alloy ingots, Advanced Engineering Materials 13 (7) (2011) 570–580.

[25] H. Nguyen-Thi, C. A. Gandin, H. Combeau, M. Založnik, M. Bellet, Finite element multi-scale modeling of chemical segregation in steel solidification taking into account the transport of equiaxed grains, Metallurgical and materials transactions A 49 (5) (2018) 1725–1748.

[26] H. D. Brody, M. C. Flemings, Solute Redistribution in Dendritic Solidification, Transaction of the Metallurgical Society of AIME 236 (May) (1966) 615–624.

[27] P. C. Carman, Fluid flow through granular beds, Transactions of the Institute of Chemical Engineering 15 (1937) 150–166.

[28] C. Beckermann, Modelling of macrosegregation: applications and future needs, International Materials Reviews 47 (5) (2002) 243–261.

[29] S. Vernède, J. A. Dantzig, M. Rappaz, A mesoscale granular model for the mechanical behavior of alloys during solidification, Acta Materialia 57 (5) (2009) 1554–1569.

[30] M. Sistaninia, A. Phillion, J.-M. Drezet, M. Rappaz, A 3-d coupled hydromechanical granular model for simulating the constitutive behavior of metallic alloys during solidification, Acta Materialia 60 (19) (2012) 6793–6803.

[31] A. Phillion, J. Desbiolles, M. Rappaz, A 3d granular model of equiaxed-granular solidification, Modeling of Casting, Welding and Advanced Solidification Processes XII, TMS Publ., Warrendale, USA (2006).

[32] Y. Feng, A. Phillion, A 3d meso-scale solidification

model for metallic alloy using a volume average approach, Materialia 6 (2019) 100329.
[33] S. Vernede, P. Jarry, M. Rappaz, A granular model of equiaxed mushy zones: Formation of a coherent solid and localization of feeding, Acta Materialia 54 (15) (2006) 4023–4034.
[34] M. Sistaninia, A. Phillion, J.-M. Drezet, M. Rappaz, Three-dimensional granular model of semi-solid metallic alloys undergoing solidification: Fluid flow and localization of feeding, Acta Materialia 60 (9) (2012) 3902–3911.
[35] Y. Feng, M. Založnik, B. Thomas, A. Phillion, Mesoscale simulation of liquid feeding in an equiaxed dendritic mushy zone, Materialia 9 (2020) 100612.
[36] H. Z. Rajani, A. Phillion, 3d multi-scale multi-physics modelling of hot cracking in welding, Materials & Design 144 (2018) 45–54.
[37] Y. Meng, B. G. Thomas, Heat-transfer and solidification model of continuous slab casting: CON1D, Metallurgical and Materials Transactions B 34 (5) (2003) 685–705.
[38] J. Sengupta, Private communication (2020).
[39] J. Fuhrmann, H. Langmach, Stability and existence of solutions of time-implicit finite volume schemes for viscous nonlinear conservation laws, Applied Numerical Mathematics 37 (1-2) (2001) 201–230.
[40] J. Ni, C. Beckermann, A volume-averaged two-phase model for transport phenomena during solidification, Metallurgical Transactions B 22 (3) (1991) 349.
[41] D. Tourret, C.-A. Gandin, A generalized segregation model for concurrent dendritic, peritectic and eutectic solidification, Acta Materialia 57 (7) (2009) 2066–2079.
[42] C. Wang, S. Ahuja, C. Beckermann, H. De Groh, Multiparticle interfacial drag in equiaxed solidification, Metallurgical and Materials Transactions B 26 (1) (1995) 111–119.
[43] J. Dongarraxz, A. Lumsdaine, X. Niu, R. Pozoz, K. Remingtonx, A sparse matrix library in c++ for high performance architectures, in: Second object oriented numerics conference, Citeseer, 1994, pp. 214–218.
[44] M. Ohno, H. Sato, Macrosegregation simulation model based on lattice-boltzmann method with high computational efficiency, International Journal of Heat and Mass Transfer 127 (2018) 561–570.
[45] J. Sengupta, J. Leung, A. Noorafkan, Calibration and validation of x-ray fluorescence technique for mapping centreline segregation on steel slabs, in: AISTech 2017 Conference Proceedings, 2017, pp. 1925–1938.
[46] J. Sengupta, A. Noorafkan, Quantifying slab centerline segregation: Mxrf eliminates sample preparation and etching procedures, in: AISTech 2018 Conference Proceedings, 2018, pp. 2637–2649.

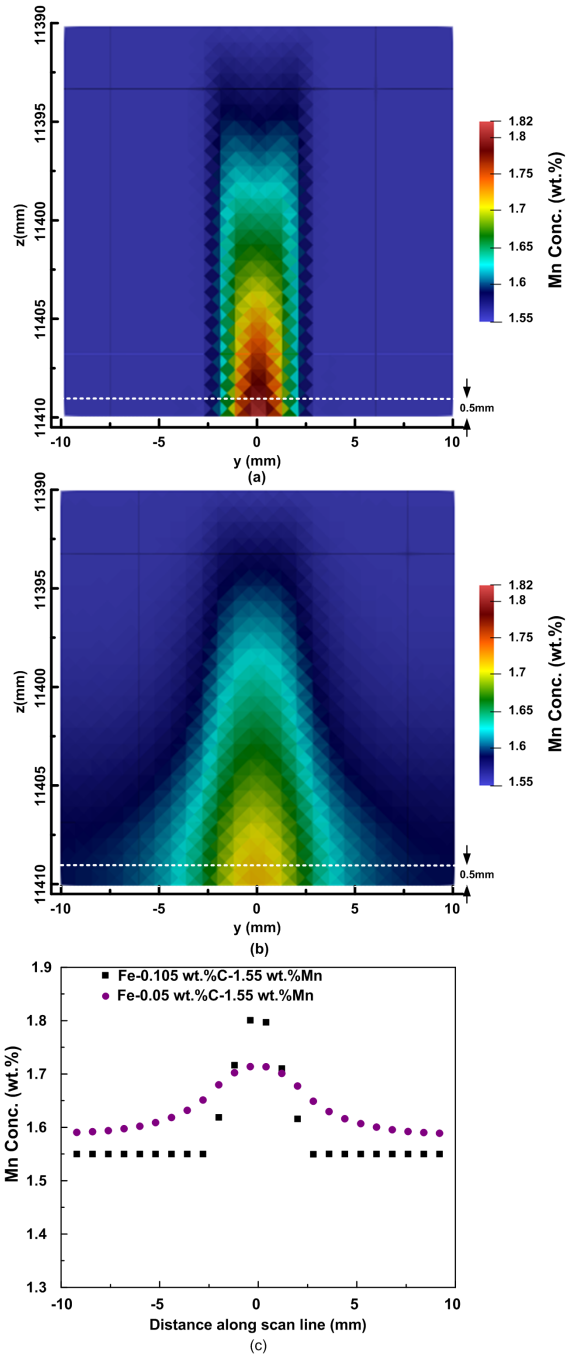

Figure 11: Influence of carbon content on the solute distribution of Mn. (a,b) Contour maps of segregation in hypo-peritectic (Fe-0.105wt.%C-1.55wt.%Mn) and non-peritectic (Fe-0.05wt.%C-1.55wt.%Mn) alloys. (c) Corresponding solute distribution along scanning line 5 mm from solidus point.

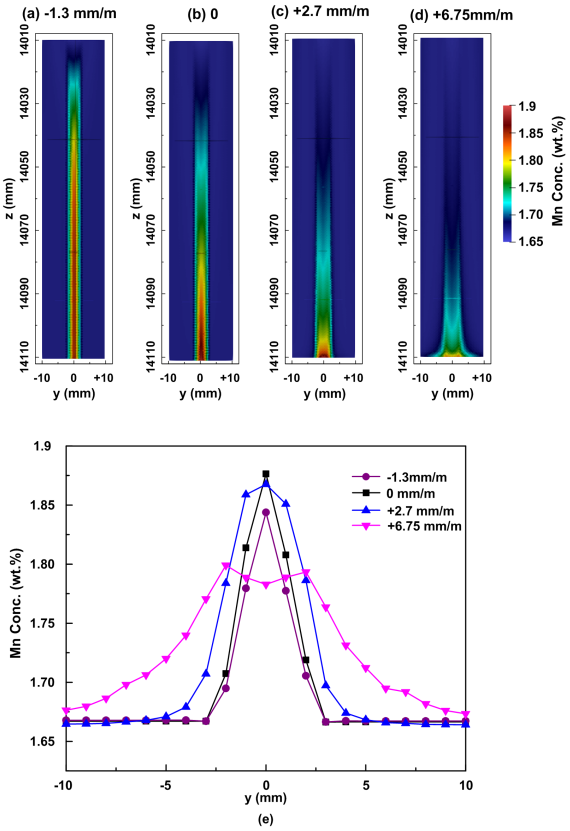

Figure 12: (a)-(d) Set of contour plots showing the influence of ESR on solute distribution; (e) Corresponding solute distribution along scanning line 5 mm from solidus point.